Journal of Applied Fluid Mechanics, Vol. 18, No. 10, pp. 2568-2580, 2025.
Available online at www.jafmonline.net, ISSN 1735-3572, EISSN 1735-3645.
https://doi.org/10.47176/jafm.18.10.3459

Numerical Simulation and Experimental Analysis of Cavitating Water Jets with Angular Nozzles under Surface Constraints

S. Li†, G. Ma, G. Li, Z. Wang, Y. Xu, Y. Yan, and J. Zhang

College of Mechanical Science and Engineering, Northeast Petroleum University, Daqing,163318, China

†*Corresponding Author Email:lisen20021225@126.com*

ABSTRACT

The effectiveness of oil pipeline cleaning is critical for minimising the frequency of reuse, and cavitation water jet technology presents a highly efficient and energy-saving cleaning method. However, the evolution behaviour of cavitation clouds under curved constraints, as well as the influence of nozzle structural parameters on cleaning performance, remains inadequately understood. In this study, high-speed imaging was employed to examine the effects of the target surface, target position, and inlet pressure on cavitation cloud evolution under curved constraints. In addition, large eddy simulation (LES) was utilised to model cavitation water jets in constrained geometries. The findings revealed that the cavitation cloud evolution cycle was shortened under curved constraints. As the target distance and inlet pressure decreased, the cavitation cloud evolution cycle, vapour phase concentration on the wall surface, and cavitation cloud width also decreased. The LES results were consistent with experimental observations. Using an orthogonal experimental design, the optimal combination of structural parameters for the angular nozzle was identified through range analysis. The results indicated that increasing the target distance led to higher vapour phase volume fraction and flow velocity on the target surface. The optimised nozzle significantly enhanced the cavitation effect at the target surface.

Article History

Received February 27, 2025
Revised May 24, 2025
Accepted May 27, 2025
Available online August 5, 2025

Keywords:

Cavitation
Turbulence simulation
Surface constraints
Structural parameter optimisation
High-speed photography

1. INTRODUCTION

Cavitation water jet technology has been widely applied in various fields, including drilling, rock fragmentation (Soyama, 2020; Świetlicki et al., 2022; Fan et al., 2024), cavitation peening to enhance metal strength, and the cleaning of ship hulls and oil tanks (Zhong et al., 2022). However, many oil pipelines are difficult to clean owing to scaling and corrosion, and removing these deposits often demands substantial manpower, resources, and time. In addition, the indirect losses caused by production shutdowns for maintenance further increase overall production costs. Therefore, studying and optimising nozzle structural parameters to determine their optimal configurations is of great importance for improving fluid jet performance and cleaning efficiency.

Many researchers have studied the transient evolution of cavitation clouds using visualisation experiments. Yang et al. (2020) employed high-speed cameras to capture unsteady flow within angular nozzles with varying diffusion angles during their investigation of cavitating jets. Through image processing, they observed the development, shedding, and collapse of cavitating water jets. Dong (2022) and Sekyi-Ansah et al. (2020) applied the finite difference method (FDM) to analyse high-speed photographic images, allowing for a clearer observation of the periodic evolution of cavitation clouds. He et al. (2023) also conducted visualisation experiments through high-speed imaging to explore the shedding frequency and underlying mechanisms of cavitation cloud formation. The findings indicated that as the pressure difference between the inlet and outlet, as well as the ambient temperature, increased, cavitation intensity became more pronounced, while the shedding frequency of cavitation clouds gradually decreased. Cui et al. (2024) used high-speed imaging to analyse the formation, development, shedding, and collapse of cavitation clouds. They revealed that higher pressure resulted in wider cavitation clouds, which reached their maximum extent during the development stage. Xu et al. (2024a) investigated the cavitation cloud characteristics produced by different nozzle types and found that angular nozzles achieved the most effective cavitation performance at an inlet pressure of 10 MPa. Liu et al. (2023) conducted both visualisation and cleaning experiments on cylindrical, organ-pipe, and

angular nozzles and found that angular nozzles produced higher velocities and more substantial cavitation clouds than the other two types. Therefore, the present study focuses on angular nozzles and aims to optimise their structural parameters.

Yuan et al. (2022) combined orthogonal experiments with deep learning methods to optimise cavitation nozzle structures based on the peak and pulsation amplitude of the impact force. Bukharin et al. (2020) designed and tested an angular nozzle for $BaSO_4$ cleaning and determined that the optimal contraction angle was 14°, while the optimal diffusion angle was 60°. Huang et al. (2024) conducted numerical simulations of the flow field inside cavitating nozzles via large eddy simulation (LES) and applied the response surface method for global optimisation of key nozzle parameters. Impact force experiments were also performed to validate the significant improvement in cavitation performance achieved by the optimised nozzle. Yang et al. (2020), through high-speed imaging and aluminium block erosion experiments, found that the diffusion angle of angular nozzles had a significant impact on cavitation and erosion intensity. The strongest cavitation effect was observed when the diffusion angle was around 60°, with different diffusion angles corresponding to different optimal target distances. Notably, nozzle structures with stronger cavitation capabilities exhibited longer optimal target distances. Liu et al. (2024), aiming to improve nozzle cleaning performance, employed a multi-objective optimisation algorithm with maximum wall static pressure, outlet velocity, and cleaning width as the optimisation criteria. The optimised nozzle demonstrated a 10% improvement in cleaning effectiveness compared with the pre-optimised design.

LES can provide more accurate simulations than Reynolds-averaged Navier–Stokes (RANS) models by directly resolving large-scale eddies while modelling smaller-scale eddies during the solution process. Trummler et al. (2020) applied the implicit LES method to study stepped nozzles and examine the factors influencing the periodic detachment of cavitation clouds. The author discovered that condensation shocks could initiate the detachment. Dai et al. (2019) used cavitation and LES models to analyse the flow characteristics and cavitation behaviour of nozzle flow fields under varying pressures and structural configurations. Han et al. (2020) employed similar numerical methods to simulate cavitating jets and investigate the interaction between cavitation and vortices. The simulated cavitation structures around the blades closely matched the experimental results. Similarly, Yang et al. (2021) used the LES model to study cavitation flow fields at high Reynolds numbers. By comparing vortex distributions at different locations, they revealed the instability phenomena of the ring vortex. Li et al. (2023) conducted a comparative analysis of LES and DES models and found that the LES model more accurately predicted the periodic detachment of cavitation clouds. Xu et al. (2024b) investigated the flow field characteristics of cylindrical cavitating nozzles under different turbulence models. They performed cavitating jet simulations using the SST k-ω model, the SBES model, and the LES model. By comparing the simulation results with high-speed imaging data, they found that both the SBES and LES models effectively predicted the dynamic evolution of cavitation clouds, with the LES model demonstrating a superior ability to capture the collapse process of cavitation clouds. Bai et al. (2021) used the LES model to analyse the periodic shedding mechanism and the shedding frequency of cavitation from both 2D and 3D perspectives. The results showed that the simulated cavitation behaviour closely matched the experimental observations.

In summary, researchers have optimised nozzle structural parameters for unconstrained conditions and larger jet target distances using computational fluid dynamics (CFD) methods and experimental approaches. It is generally accepted that an angular nozzle with a diffusion angle of 60° and a contraction angle of 13.5° produces better cavitation effects. The LES model provides an effective representation of cavitation jet flow fields. However, research on cavitation jets under curved constraints remains limited. Building on previous studies of angular cavitation nozzle structures and their flow fields, this study uses experimental methods to capture the evolution characteristics of cavitation clouds. This study comparatively analyses the differences in cavitation flow fields at various jet target distances and then compares the experimental results with numerical simulation outcomes. Using numerical simulation methods, the study optimises the angular nozzle structure parameters under curved constraints for low-pressure conditions at 10 MPa and identifies the optimal nozzle structure for curved constraints. These findings provide a theoretical basis for the application of cavitation water jet technology in tubing cleaning.

2. EXPERIMENTAL SYSTEM AND GEOMETRICAL MODEL

2.1. Experimental System

An experimental platform for cavitating water jets constrained by curved surfaces was developed. The platform included a high-speed camera, a water tank, LED lights, a plunger pump, a pressure gauge, a relief valve, nozzles, target objects, and a support frame, as illustrated in Fig. 1 The LED lights and high-speed camera were positioned along the same axis. During the experiment, the data acquisition system recorded and stored the images captured by the high-speed camera for later analysis.

To investigate the evolution patterns of cavitation clouds generated by angular nozzles in confined curved spaces, explore their formation mechanisms and distribution characteristics, and analyse the influence of curved surfaces on the morphology and evolution of cavitation clouds, a high-speed camera was used to capture the cavitation phenomena in the observation area. The underwater experimental setup was created in a plexiglass tank measuring 600 mm in length, 400 mm in width, and 800 mm in height, with the nozzle positioned 300 mm below the water surface. The tank was equipped with both a drain and an inlet. The inlet circulated cooling

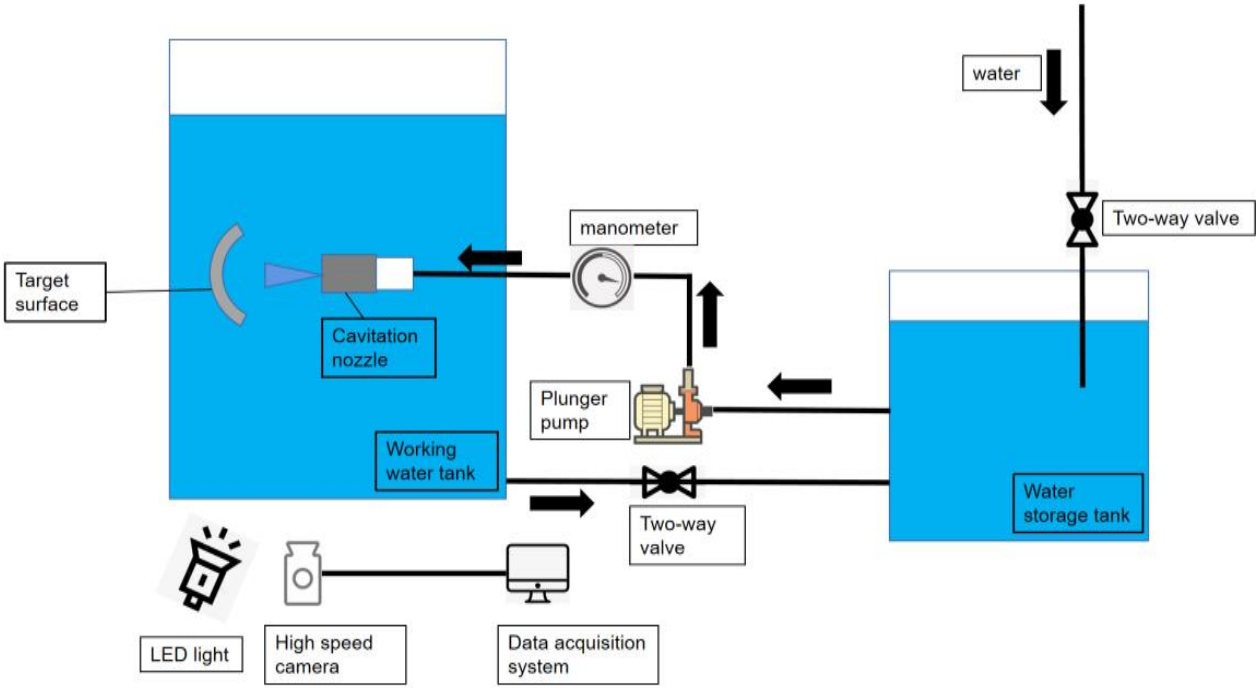

Fig. 1 Cavitating jet experimental system

Table 1 Structural parameters of the angular nozzle (units: mm)

Type of structure	D	d	L1	L2	L3	β	θ
Size	6	1	5	4	4	13.5°	60°

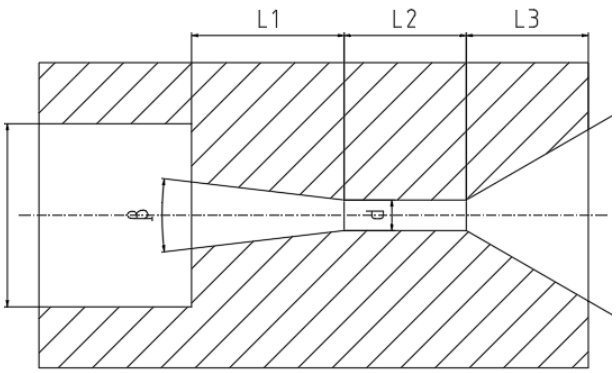

Fig. 2 Angular nozzle structure

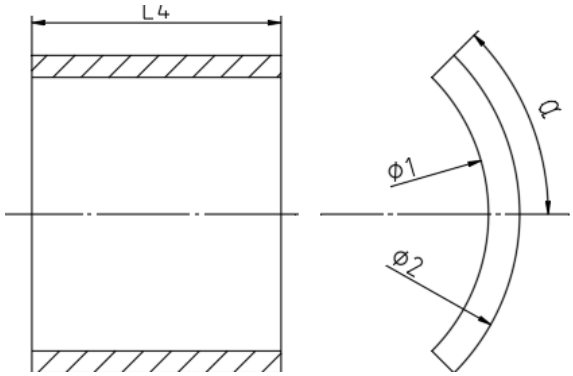

Fig. 3 Structure of a curved surface target

water to control the temperature, while the drain maintained a stable water level during the experiment, minimising interference with the cavitation jet. Tap water, left standing for 24 hours prior to the experiment, was used. During testing, an electronic thermometer recorded water temperatures of 18°C–20°C (with a maximum error of ±1°C), which was found to be the optimal temperature range for the experimental objectives. The high-speed camera was set with an exposure time of 0.1 ms and a frame rate of 10,000 fps. Recording began once cavitation cloud development reached stable periodicity, with each capture lasting over 1 second. A curved target with an inner diameter of 62 mm was chosen. At an inlet pressure of 10 MPa, standoff distances of 12 mm, 15 mm, and 18 mm were tested to observe variations in cavitation clouds. Additionally, with a fixed standoff distance of 15 mm, inlet pressures of 7 MPa, 10 MPa, and 12 MPa were applied to examine pressure-induced changes in cavitation cloud behaviour.

2.2. Geometrical Model

Building on previous research on nozzle structures and practical cleaning applications, the initial nozzle design was established. The structural parameters are presented in Table 1, Fig. 2 and 3 illustrate the structures of the nozzle and the curved surface target, respectively.

2.3 Orthogonal Experimental Design

Orthogonal experimental design leverages orthogonality to select representative points for testing. It is an efficient method that requires a relatively small number of experiments to determine the optimal combination

Table 2 Factor levels

Level	Factors			
	A contraction section L_1/(mm)	B cylindrical section L_2/(mm)	C diffusion section L_3/(mm)	D target distance L/(mm)
1	3	2	2	8
2	4	3	3	10
3	5	4	4	12
4	6	5	5	15

of structural parameters.

The flow field of the nozzle is mainly influenced by its geometric dimensions. Numerical simulation analysis, combined with orthogonal experimental methods, enables more accurate identification of the optimal structural parameters for the angular nozzle. Considering the impact of geometric parameters of the angular nozzle on cavitation effects and previous optimisation research, the nozzle inlet diameter (D) is set at 6 mm, the contraction angle (β) at 13.5, the diffusion angle (θ) at 60°, and the cylindrical segment diameter (d) at 1 mm. Four parameters are selected as experimental factors: the length of the nozzle contraction section, the length of the cylindrical section, the length of the diffusion section, and the jet target distance. Each factor is set at four levels, as shown in Table 2 Numerical simulations for 16 experimental groups are conducted using the LES method. Range analysis of the experimental data is performed to identify the optimal parameter combination. The cavitation effectiveness is assessed by measuring the maximum vapour phase volume fraction and the peak flow velocity at the target surface.

3. CFD METHOD AND SIMULATION

3.1. Governing Equations

Fluent, the fluid simulation software, offers three multiphase flow models: the VOF model, the mixture model, and the Euler model. The VOF model is mainly used for simulating individual cavitation bubbles and is not suitable for the macroscopic cavitation phenomena addressed in this study. While the Euler model provides higher computational accuracy than the mixture model, it demands more computational power. Given considerations of computational accuracy, convergence, and resource requirements, the mixture model is selected for the simulations in this research.

The mass conservation equation for the mixture model in a Cartesian coordinate system can be expressed as follows:

$$\frac{\partial(\rho_m)}{\partial t}+\nabla(\rho_m\vec{v}_m)=\overline{m} \tag{1}$$

$$\begin{aligned}&\frac{\partial}{\partial \mathrm{t}}(\rho_m\vec{v}_m)+\nabla(\rho_m\vec{v}_m\vec{v}_m)=-\nabla P\\&+\nabla[\mu_m(\nabla\vec{v}_m+\nabla\vec{v}_m^T)]+\rho_m\vec{g}_m\\&+\vec{F}+\nabla\cdot(\sum_{k=1}^{n}\alpha_k\rho_k\vec{v}_{dr,k}\vec{v}_{dr,k})\end{aligned} \tag{2}$$

where ρ_m is the mixture density, $\vec{v}_m$ is the mass-averaged velocity, $\overline{m}$ is the mass exchange, $\vec{F}$ is the body force, μ_m is the mixture viscosity, and $\vec{v}_{dr,k}$ is the second drift velocity.

3.2. Cavitation Model

In this study, the Zwart–Gerber–Belamri cavitation model is applied. The equation for this model is as follows:

If $P \le P_v$,

$$R_c = F_{vap}\frac{3\alpha_{nuc}(1-\alpha_v)\rho_v}{R_B}\sqrt{\frac{2}{3}\frac{P_v-P}{\rho_l}} \tag{3}$$

If $P > P_v$,

$$R_c = F_{cond}\frac{3\alpha_v\rho_v}{R_B}\sqrt{\frac{2}{3}\frac{P-P_v}{\rho_l}} \tag{4}$$

where R_B is the bubble radius, R_B =10^{-6} m; P_v is the saturation vapour pressure; P is the local far-field pressure; α_{nuc} is the volume fraction of the nucleation site, α_{nuc}=5×10^{-4}; ρ_l is the density of the liquid phase; F_{vap} is the evaporation coefficient, F_{vap}=70; and F_{cond} is condensation coefficient, F_{cond}=0.015.

3.3. Turbulence Model

The Large Eddy Simulation (LES) model employs a spatial averaging method to deal with turbulent fluctuations. By applying a filtering function, it differentiates large-scale eddies that are directly simulated from small-scale eddies that are modeled to achieve closure. The LES model enables a better capture of the characteristics of the flow field. Before conducting Large Eddy Simulation, a stable flow field must first be calculated using the Renormalization Group (RNG) k-ε model, which can enhance the convergence rate of the LES model.

Cavitating jets consist of a two-phase flow, with water vapour representing the vapour phase and liquid water constituting the liquid phase. The saturation vapour pressure is 3169 Pa. For the numerical simulation, a double-precision, pressure-based solver is used. The inlet pressure is set at 10 MPa, the outlet pressure at 0 MPa, the Reynolds number is 2.8 × 10^6, and the jet target distance is 15 mm. The coupled algorithm is selected for velocity-pressure coupling, with a time step of 10^{-5} seconds. The convergence criterion is set to 10^{-5}, with

Table 3 Simulation method settings

Turbulence model	RNG k-e 模型	LES 模型
Pressure–velocity coupling method	Coupled	Coupled
Gradient interpolation scheme	Least squares cell-based	Least squares cell-based
Pressure interpolation scheme	PRESTO!	PRESTO!
Convection discretisation scheme	Second-order upwind	Second-order upwind
Volume fraction interpolation scheme	First-order upwind	First-order upwind
Transient formulation	First-order upwind	Bounder second-order implicit
Convergence criterion	1×10^{-5}	1×10^{-5}

each time step requiring 20 internal iterations. Pressure–velocity coupling is implemented using the coupled algorithm. The simulation method settings are shown in Table 3.

RNG k–ε Model

The governing equations of the RNG k–ε model are as follows:

$$\frac{\partial(\rho k)}{\partial t}+\frac{\partial(\rho k u_i)}{\partial x_i}=\frac{\partial}{\partial x_j}\left[a_k\mu_{eff}\frac{\partial k}{\partial x_j}\right] \tag{5}$$
$$+G_k+G_b-\rho\varepsilon-Y_M+S_k$$

$$\frac{\partial(\rho\varepsilon)}{\partial t}+\frac{\partial(\rho\varepsilon u_i)}{\partial x_i}=\frac{\partial}{\partial x_j}\left[a_\varepsilon\mu_{eff}\frac{\partial \varepsilon}{\partial x_j}\right] \tag{6}$$
$$+\frac{C_{1\varepsilon}}{k}(G_k+C_{3\varepsilon}G_b)-C_{2\varepsilon}\rho\frac{\varepsilon^2}{k}-R_\varepsilon+S_\varepsilon$$

The viscosity expression is given by

$$\mu_{eff}=\mu+\mu_t \tag{7}$$

$$R_\varepsilon=\frac{C_\mu\rho\eta^3\left(1-\frac{\eta}{\eta_0}\right)}{1+\beta\eta^3}\frac{\varepsilon^2}{k} \tag{8}$$

The strain rate tensor is defined as

$$\eta=\left(2E_{ij}\cdot E_{ij}\right)^{\frac{1}{2}} \tag{9}$$

$$\frac{k}{\varepsilon}E_{ij}=\frac{1}{2}\left(\frac{\partial u_i}{\partial x_j}+\frac{\partial u_j}{\partial x_i}\right) \tag{10}$$

where η is the turbulent viscosity coefficient; G_k is the turbulent kinetic energy generation term due to mean velocity gradients, J; G_b is the turbulent kinetic energy generation term due to buoyancy, J; Y_M represents the fluctuations caused by excessive diffusion in compressible turbulence, m; and $C_{1\varepsilon}, C_{2\varepsilon}, C_{3\varepsilon}$ C_μ are the empirical constants, with $C_{1\varepsilon}$=1.42, $C_{2\varepsilon}$=1.68, $C_{3\varepsilon}$ =1.64, and C_μ =0.09.

LES Model

The LES model uses a filtering function to separate vortices of different scales, directly simulating the larger-scale vortices while modelling the smaller-scale vortices through control equations that link them to the larger-scale vortices. The filtering equation is as follows:

$$\frac{\partial\rho}{\partial t}+\frac{\partial}{\partial x_i}(\rho\bar{u_i})=0 \tag{11}$$

$$\frac{\partial}{\partial t}\left(\rho\bar{u_i}\right)+\frac{\partial}{\partial x_i}\left(\rho\bar{u_i}\bar{u_j}\right)=-\frac{\partial}{\partial x_i} \tag{12}$$
$$+\frac{\partial}{\partial x_i}\left(\mu\frac{\partial\bar{u_i}}{\partial x_j}\right)-\frac{\partial\tau_{ij}}{\partial x_j}$$

$$\tau_{ij}=-\mu_t\bar{S}_{ij}+\frac{1}{3}\tau_{kk}\delta_{ij} \tag{13}$$

In this study, the wall-adapting local eddy-viscosity (WALE) model within LES is used. The turbulent viscosity μ_t and the subgrid-scale mixing length L_s are defined as follows:

$$\mu_t=\rho_m L_s^2\frac{(s_{ij}^d s_{ij}^d)^{3/2}}{(\bar{s}_{ij}\bar{s}_{ij})^{5/2}+(s_{ij}^d s_{ij}^d)^{5/4}} \tag{14}$$

$$L_s=\min(\kappa d, C_w V^{1/3}) \tag{15}$$

$$S_{ij}^d=\frac{1}{2}(\bar{g}_{ij}^2+\bar{g}_{ji}^2)-\frac{1}{3}\delta_{ij}\bar{g}_{kk}^2 \tag{16}$$

$$\bar{g}_{ij}=\frac{\partial\bar{u_i}}{\partial x_i} \tag{17}$$

where ρ is the fluid density, (kg/m³), $\bar{u_i}$ and $\bar{u}_j$ are the fluid velocities, (m/s), $\bar{p}$ is the fluid static pressure, (Pa), τ_{ij} is the subgrid-scale stress, and C_w = 0.325 is the WALE model constant.

3.4 Computational Domain and Grid

To ensure fully developed inlet flow at the nozzle entrance, the inlet length is set to 20 mm, which is 3 to 5 times the inlet diameter. To minimise the impact of model boundaries and outlet flow recirculation on the core jet velocity under curved surface constraint conditions, a hexahedral fluid computational domain with dimensions of 80 mm in length, width, and height is used. The fluid computational domain for the choked jet flow in the angular nozzle under curved surface constraint conditions is illustrated in Fig. 4.

The flow field is meshed using ICEM software, with a refined mesh applied within the nozzle and along the inner wall of the target surface. To ensure mesh independence, this study compares the time-averaged vapour volume fraction (Fig. 5) and the velocity variation

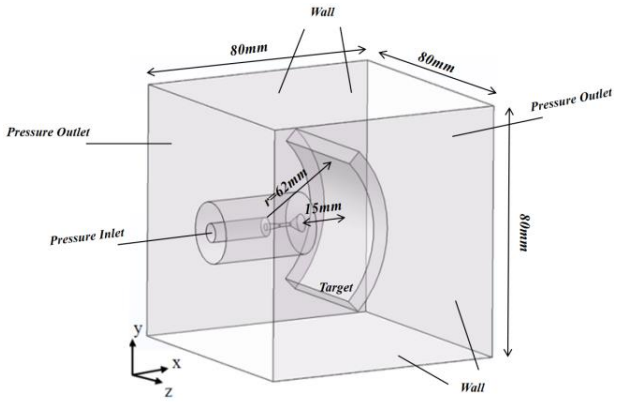

Fig. 4 Fluid space model

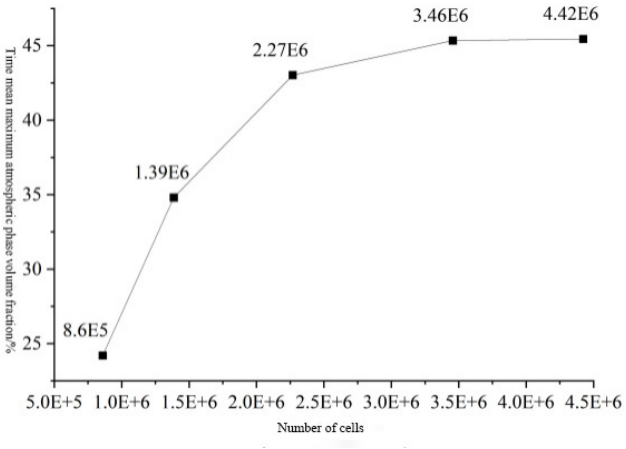

Fig. 5 Time-averaged vapour phase volume fraction

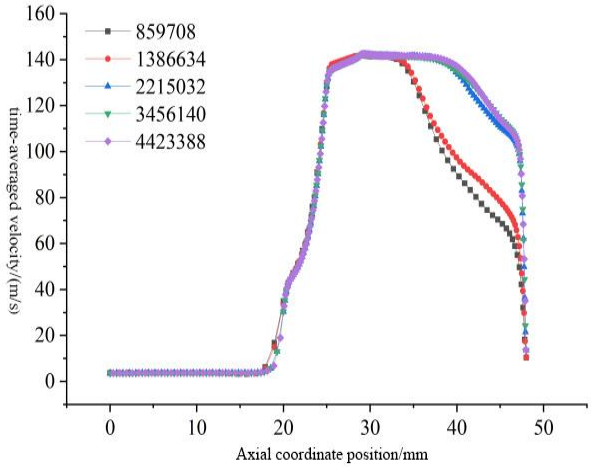

Fig. 6 Average velocity along the axial direction

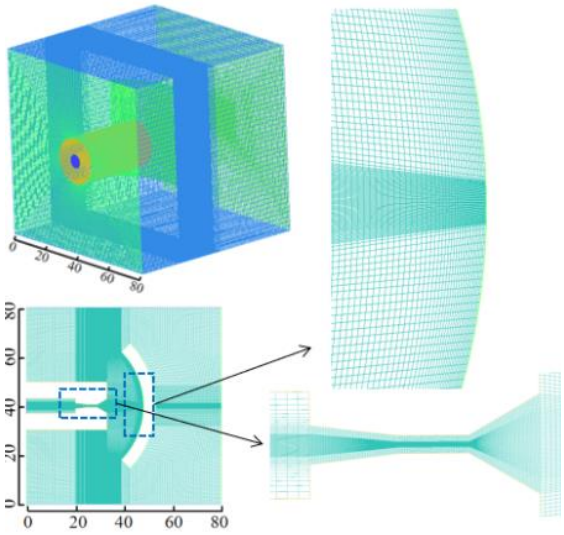

Fig. 7 Mesh configuration of the angular nozzle structure

along the axial direction (illustrated in Fig. 6) under different mesh densities. This approach, commonly used in related studies, relies on the stability of the vapour volume fraction and velocity distribution to assess whether the mesh is adequately refined (Wang et al., 2024; Wang et al., 2025). Consequently, this study adopts vapour volume fraction and velocity as key indicators for evaluating mesh independence.

When the number of grid cells exceeds 3.45 million, variations in both the average maximum vapour volume fraction within the fluid domain and the velocity along the nozzle axis become negligible. According to Wang's study (Wang et al., 2025), under a similar fluid domain volume, a grid count of 3.45 million is sufficient to meet computational accuracy requirements. Therefore, the final grid count is set at approximately 3.45 million (Fig. 7).

4. RESULTS AND DISCUSSION

4.1 Analysis of Experimental Results

The evolution of cavitation clouds was captured using high-speed cameras under the following conditions:

a fixed inlet pressure of 10 MPa with varying jet target distances of 12 mm, 15 mm, and 18 mm; a fixed jet target distance of 15 mm with varying inlet pressures of 7 MPa, 10 MPa, and 12 MPa; and during free jet flow from the nozzle.

MATLAB was used to convert high-speed camera images into grayscale matrices. The frame difference method (FDM) was applied to evaluate cavitation cloud formation and dissipation by calculating the grayscale differences between consecutive images. In the FDM visualisations, red areas represent cavitation cloud formation, while blue areas indicate dissipation. This method, combined with high-speed imaging, offers a more intuitive representation of the flow field characteristics associated with cavitation clouds.

The evolution of cavitation clouds at different jet target distances under a fixed inlet pressure of 10 MPa is illustrated in Fig. 8 The process can be divided into four stages: initiation, growth, detachment, and collapse of the cavitation cloud (He et al., 2023). At a target distance of 12 mm, cavitation cloud detachment begins at 0.1 ms, followed by continuous expansion from 0.1 ms to 0.5 ms, culminating in collapse upon contact with the wall. The

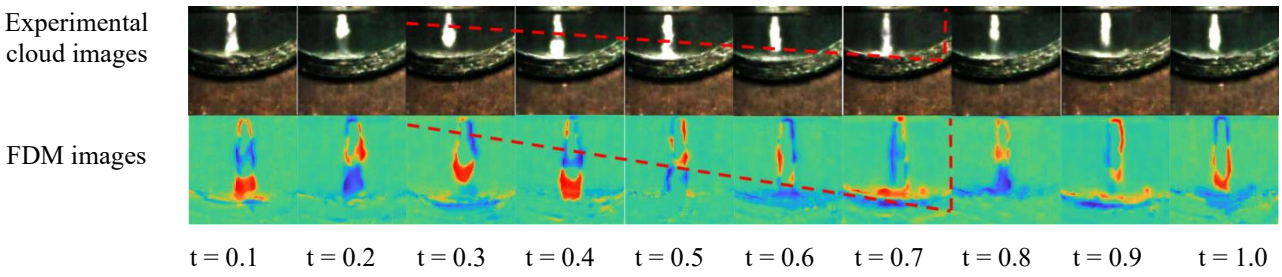

(a) Evolution of cavitation clouds at a target distance of 12 mm

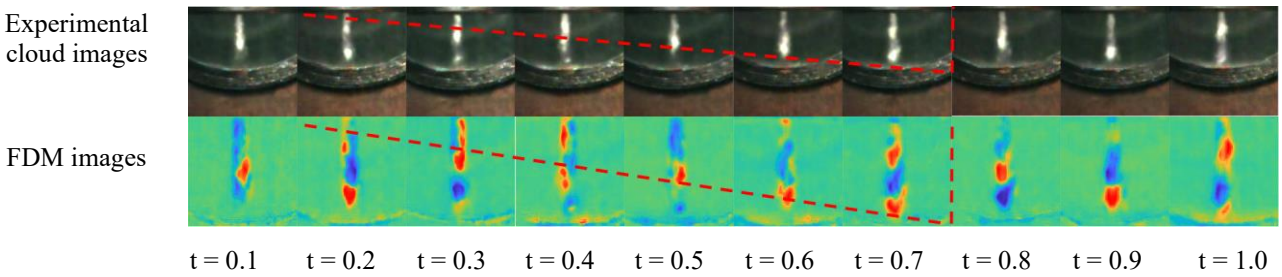

(b) Evolution of cavitation clouds at a target distance of 15 mm

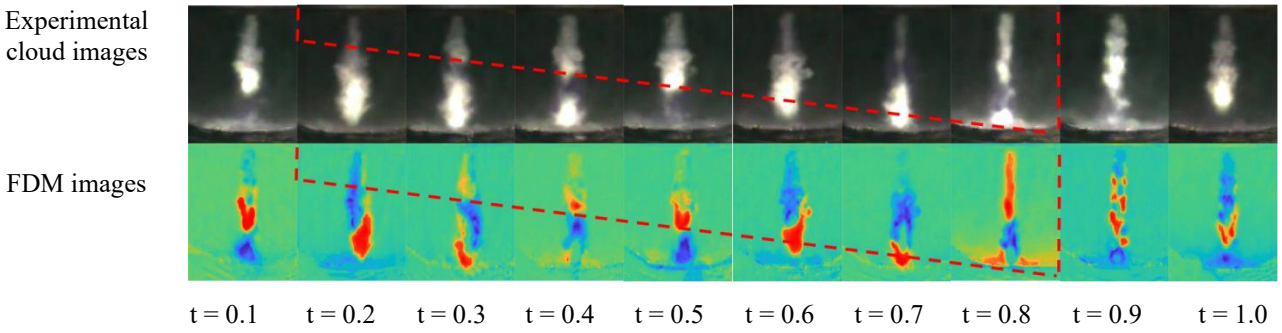

(c) Evolution of cavitation clouds at a target distance of 18 mm

Fig. 8 Evolution of Cavitation Clouds at Different Jet Target Distances

full development cycle lasts approximately 0.5 ms. Similar patterns are observed at target distances of 15 mm and 18 mm, with development cycles of approximately 0.6 ms and 0.7 ms, respectively. Greater target distances result in more extensive cavitation cloud formation, increased vapour concentration, and a broader impact area on the target surface.

In experiments conducted at a nozzle-to-target distance of 15 mm under inlet pressures of 7, 10, and 12 MPa, the evolution of cavitation clouds follows a pattern similar to that illustrated in Fig. 9 displaying four distinct stages of development.

When the inlet pressure is set to 7 MPa, the cavitation cloud development period is approximately 0.4 ms. As the pressure increases to 10 MPa, the nozzle exit velocity increases, leading to a longer cavitation cloud development cycle. The cavitation cloud at 10 MPa has a significantly larger diameter than that at 7 MPa. Higher jet velocities enhance cavitation cloud formation, resulting in greater vapour concentration and a wider diffusion range upon impact with the target surface, with a development period of about 0.6 ms.

At an inlet pressure of 12 MPa, the cavitation effect becomes even more pronounced as both pressure and velocity increase (Xiang et al., 2020). Under these conditions, the cavitation cloud's development cycle is approximately 0.7 ms. This study shows that the developmental cycle of cavitation clouds in narrow spaces constrained by curved surfaces is directly proportional to jet pressure, with higher pressures resulting in longer developmental cycles.

In the case of unrestricted free jet flow from an angular nozzle, the evolution of cavitation clouds is illustrated in Fig. 10. At t = 0.1 ms, cavitation clouds begin to emerge continuously from the nozzle outlet, maintaining a relatively narrow width. By t = 0.2 ms, a new cavitation cloud forms at the nozzle outlet. From t = 0.3 ms to t = 1.0 ms, the cavitation cloud progresses downstream and expands. As the cavitation cloud in the upstream sections grows, the detached portions in the downstream sections gradually shrink and collapse. For the unrestricted angular nozzle free jet flow, new cavitation pulses appear at 1 ms intervals, with a period of 0.9 ms.

The experimental results show that the cavitation cloud development follows a periodic pattern, regardless of whether the nozzle outlet is constrained (Peng et al., 2021) However, surface constraints, especially target distance and pressure, have a notable

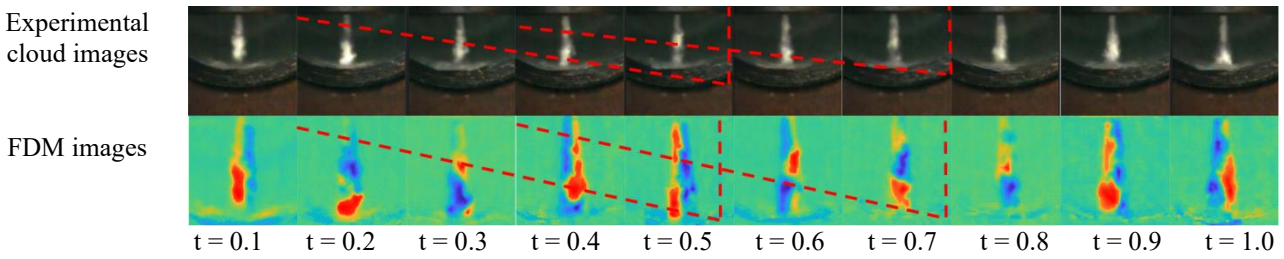

(a) Evolution of cavitation clouds at an inlet pressure of 7 MPa

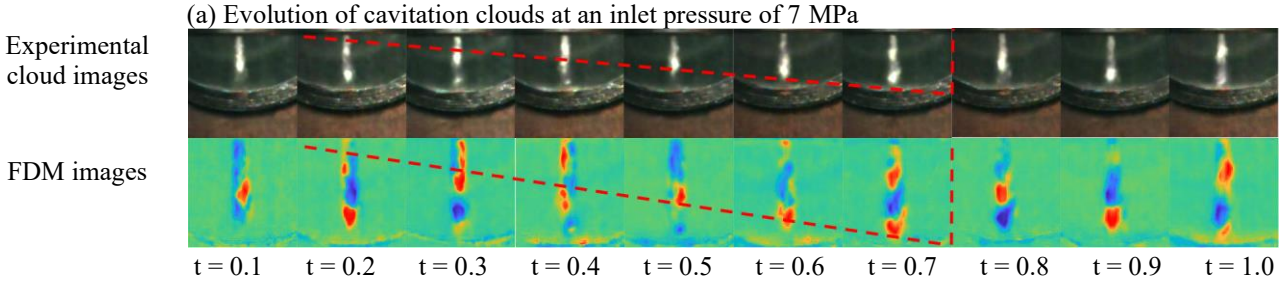

(b) Evolution of cavitation clouds at an inlet pressure of 10 MPa

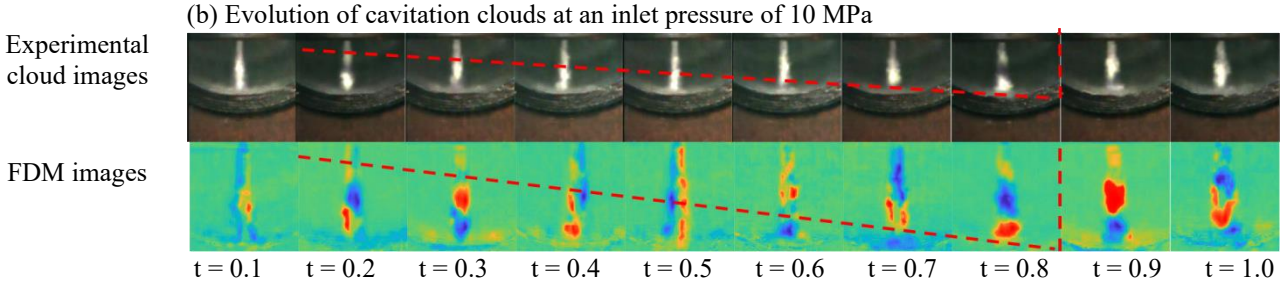

(c) Evolution of cavitation clouds at an inlet pressure of 12 MPa

Fig. 9 Evolution of cavitation clouds at different inlet pressures

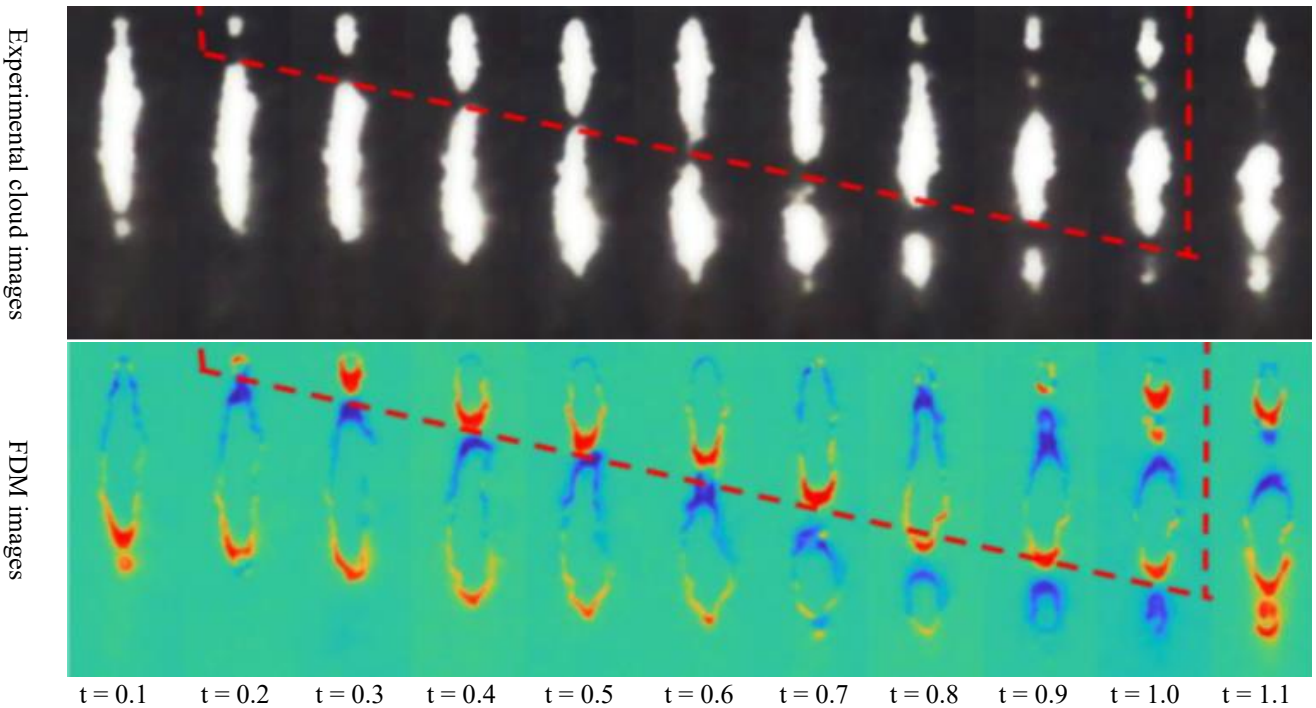

Fig. 10 Evolution of cavitation clouds in free jets

effect on the cavitation cloud cycle. Smaller target distances and lower pressures result in a shorter cavitation cloud evolution cycle and a reduced width.

Surface constraints modify the flow field of the nozzle jet, requiring optimisation of nozzle structural parameters to suit these conditions. Optimised cavitation nozzles can improve efficiency in narrow spaces constrained by curved surfaces, such as enhancing pipeline cleaning effectiveness and increasing pipeline reusability.

4.2 Comparison of LES numerical Modelling and Experiment

The results of the LES modelling are compared with experimental observations at the same time in Fig. 11.

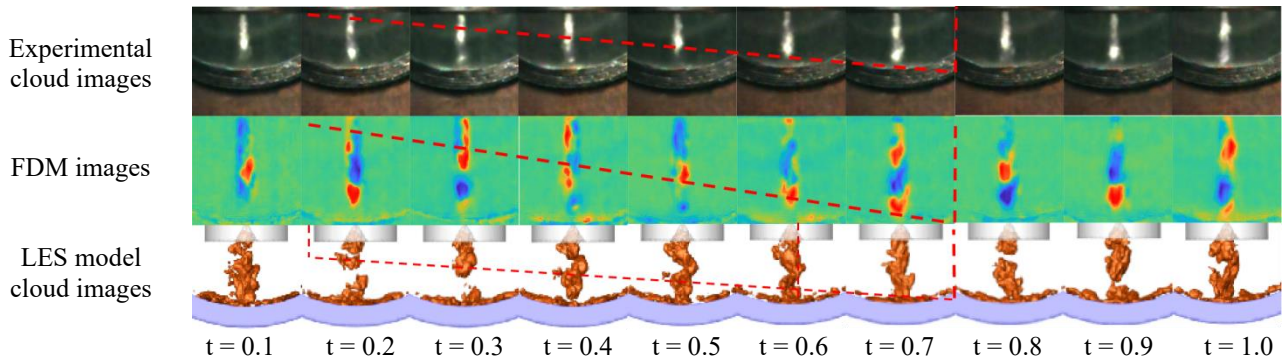

Fig. 11 Comparison of simulation results with experimental observations

The LES model effectively captures the transient characteristics of cavitation phenomena (Xu et al., 2024b): at 0.2 ms, cavitation clouds begin to detach, and new cavitation clouds start to form. Between 0.2 ms and 0.7 ms, the previous cavitation clouds enter the collapse phase while new clouds continue to develop. Upon impacting the target surface, these clouds spread outward from the centre and gradually collapse. At 0.7 ms, another cavitation cloud detachment occurs, with an instantaneous evolution cycle of approximately 0.6 ms.

A comparison of the experimental and simulation results reveals that the morphology and evolution cycles of cavitation clouds in the LES model closely match the experimental observations. This agreement demonstrates that the LES model effectively simulates the cavitating water jet flow field.

4.3 Analysis of Orthogonal Experimental Results

Numerical LES was used to study 16 experimental setups based on orthogonal experimental methods. The optimal parameter combination was determined through range analysis of the experimental indicators. Cavitation occurrence was assessed by measuring the maximum vapour volume fraction and the maximum velocity at the target surface. A higher vapour volume fraction at the target surface indicates more cavitation bubble formation and stronger cavitation effects, leading to a greater impact force from bubble collapse on the target surface (Shan et al., 2024) Higher flow velocities enhance cavitation effects, as cavitation bubbles are more likely to collapse under high-speed flow, generating stronger impact forces. The orthogonal experimental design and corresponding results are presented in Table 4.

The extreme difference analysis of the time-averaged maximum vapour volume fraction is presented in Table 5 This analysis ranks the primary and secondary factors influencing the maximum vapour volume fraction at the target surface, considering parameters such as target distance, cylinder section length, diffuser section length, and contraction section length.

The average values of the four factors at their respective levels are illustrated in Fig. 12 Factor D is identified as the primary influence on the maximum

Table 4 Orthogonal experimental design and results

No.	Factors				Maximum vapour volume fraction on the target surface (%)	maximum jet velocity at the target surface (m/s)
	A	B	C	D		
1	1	1	1	1	96.3	153.2
2	1	2	2	2	96.8	155.0
3	1	3	3	3	96.6	161.1
4	1	4	4	4	98.2	157.0
5	2	1	2	3	97.4	156.2
6	2	2	1	4	98.1	169.4
7	2	3	4	1	97.6	158.6
8	2	4	3	2	94.9	162.8
9	3	1	3	4	98.1	164.1
10	3	2	4	3	97.5	161.1
11	3	3	1	2	96.0	158.6
12	3	4	2	1	95.5	157.4
13	4	1	4	2	97.5	164.9
14	4	2	3	1	97.0	160.9
15	4	3	2	4	96.8	163.4
16	4	4	1	3	96.0	154.5

Table 5 Analysis of the extreme difference in maximum vapour volume fraction

Index	A	B	C	D
K_1	387.9	389.3	386.4	386.4
K_2	388	389.4	386.5	385.2
K_3	387.1	387	386.6	387.5
K_4	387.3	384.6	390.8	391.2
k_1	96.975	97.325	96.6	96.6
k_2	97	97.35	96.625	96.3
k_3	96.775	96.75	96.65	96.875
k_4	96.825	96.15	97.7	97.8
R	0.225	1.2	1.1	1.5
Primary and Secondary Factors	D>B>C>A			

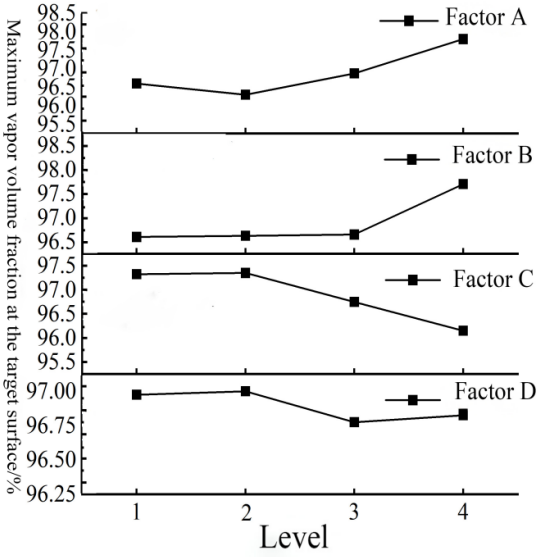

Fig. 12 Impact of each factor on the maximum vapour volume fraction at the target surface

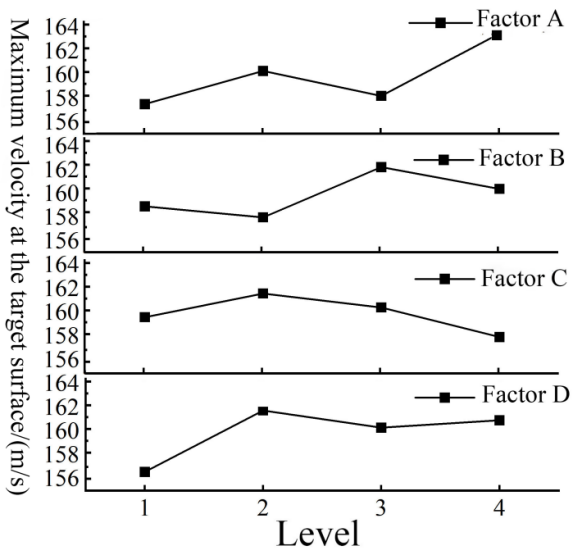

Fig. 13 Impact of each factor on the maximum velocity at the target surface

Table 6 Extreme difference analysis of maximum velocity

Index	A	B	C	D
K_1	626.3	638.4	635.7	630.1
K_2	647	646.4	632	641.3
K_3	641.2	641.7	648.9	632.9
K_4	643.7	631.7	641.6	653.9
k_1	156.575	159.6	158.925	157.525
k_2	161.75	161.6	158	160.325
k_3	160.3	160.425	162.225	158.225
k_4	160.925	157.925	160.4	163.475
R	5.175	3.675	4.225	5.95
Primary and Secondary Factors	D>A>C>B			

vapour volume fraction at the target surface, reaching its peak at level 4. Increasing the length of the diffuser section (Factor C) is associated with higher average vapour volume fractions, peaking at level 4. Both Factors B and A reach their maximum vapour volume fractions at level 2. Thus, to optimise the maximum vapour volume fraction as a performance metric, the optimal combination is $A_2B_2C_4D_4$.

The extreme difference analysis of the maximum velocity is presented in Table 6. The factors influencing the maximum velocity at the target surface are ranked in order of significance: target distance, contraction section length, diffuser section length, and cylinder section length.

The average values of the four factors across their respective levels are illustrated in Fig. 13 Factor D has the most significant impact on the maximum velocity at the target surface, playing a crucial role in cavitation effects. Factor C peaks at level 3, while Factors B and A reach their maximum velocity at level 2. Consequently, the optimal combination for maximising velocity as a performance metric is $A_2B_2C_3D_4$.

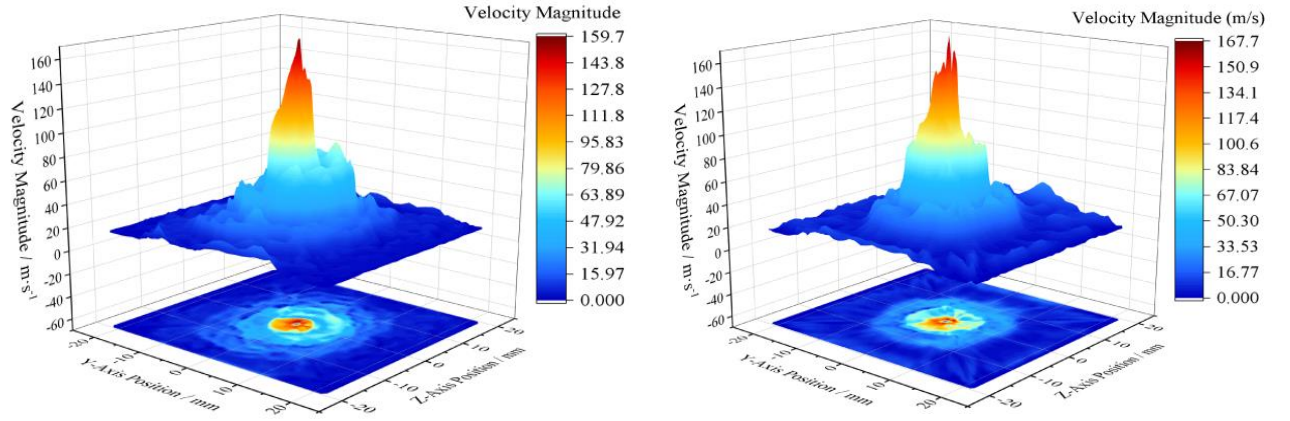

(a) Before optimisation (b) After optimisation

Fig. 14 Velocity distribution on the target surface

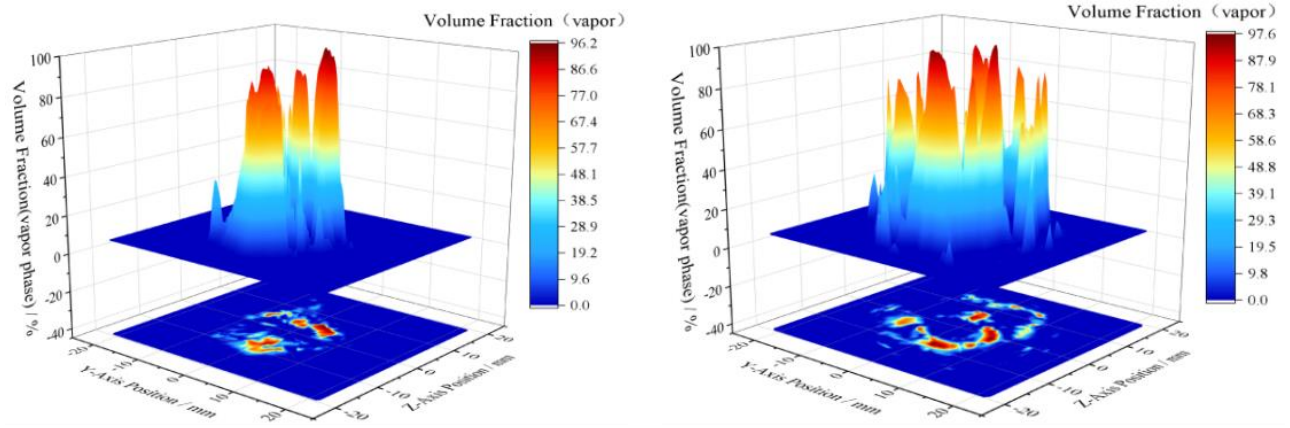

(a) Before optimisation (b) After optimisation

Fig. 15 Distribution of water vapour volume fraction on the target surface

In environments with curved surfaces and limited space, increasing the distance to the target improves both the maximum vapour volume fraction and the peak velocity at the target surface. For the design of the angular nozzle, setting the contraction section length (Factor A) to 4 mm (level 2) provides the highest values for both maximum velocity and vapour volume fraction, making A_2 the optimal choice. Factor B has the most significant influence on the vapour volume fraction, with a secondary effect on velocity. Considering that the vapour volume fraction is a key indicator of cavitation intensity, B_2 is the preferred option. Factor C has a smaller effect on both vapour volume fraction and velocity, but because velocity affects impact force, C_3 is selected as the best result. Therefore, the optimal configuration for the angular nozzle is $A_2B_2C_3$.

4.4 Comparative Analysis of Flow Fields Before and After Structural Optimisation

Figure 14 illustrates the velocity contour plots at the point of maximum velocity on the target surface, both before and after the structural optimisation of the angular nozzle. First, the maximum velocity at the target surface is 159.7 m/s. After optimisation, this value increases to 167.7 m/s. The figure shows that after optimisation, there are more velocity peaks and a larger high-speed flow region on the target surface. Consequently, the optimised nozzle generates a jet with higher velocity and a broader coverage area on the target surface, leading to greater impact force and improved cleaning efficiency.

Figure 15 illustrates the distribution of vapour volume fraction on the target surface. The data reveal a significant increase in the maximum vapour volume fraction following optimisation. First, the maximum volume fraction is 96.24%, which increases to 97.63% after optimisation. When the vapour volume fraction peaks at the target surface, the optimised nozzle design generates a larger vapour phase area. Both the maximum vapour volume fraction and the extent of cavitation clouds on the target surface are critical factors in determining the nozzle's cleaning efficiency and the effective cleaning area. Therefore, the optimisation greatly enhances the cavitation performance of the angular nozzle.

5. CONCLUSION

This paper presents a comparative analysis of cavitation cloud morphology and evolution under free jet and curved surface constraint conditions, along with experimental and LES simulation results. According to a four-factor, four-level orthogonal experimental design for structural parameter optimisation of an angular nozzle, the following conclusions are drawn:

1. Under curved surface constraints, both the

evolution period and width of the cavitation cloud are reduced. Smaller target distances and lower pressures result in reduced evolution periods, lower vapour phase concentrations, and narrower widths on the target surface.

2. A comparative analysis of the cavitation cloud at a 15 mm target distance shows that the morphology and evolution period simulated by the LES model closely match experimental observations under curved surface constraint conditions. The LES model effectively captures the cavitation jet flow characteristics of the angular nozzle under these conditions.

3. Using LES numerical simulation methods and a four-factor, four-level orthogonal experimental design, optimal structural parameters are obtained through extreme difference analysis: contraction section length L1 = 4 mm, cylinder section length L2 = 3 mm, and diffuser section length L3 = 4 mm.

4. After optimisation, the angular nozzle structure generates higher maximum velocity upon impact at the target surface, larger areas of high-speed regions, higher maximum vapour volume fractions, and larger vapour phase areas compared with the original structure. Consequently, the optimised cavitation effect is superior, leading to an increased effective cleaning area and improved efficiency, which is beneficial for pipeline cleaning.

The optimized nozzle structure is more suitable for cleaning under the conditions of oil pipelines. In the future, actual oil pipe cleaning experiments will be conducted using the high-speed imaging experimental platform. By comparing the cleaning performance of the optimised nozzle with that of the original nozzle structure, the reliability of the optimisation results will be verified.

ACKNOWLEDGEMENTS

This study was funded by the National Natural Science Foundation of China (grant no. 11402051), and the Natural Science Foundation of Heilongjiang (grant no. LH2022A004, LH2022E016).

We also thank the NativeEE (www.nativeee.com), which offered an English editing service.

CONFLICT OF INTEREST

The authors declare no conflict of interest.

AUTHORS CONTRIBUTION

Sen Li: Conceptualisation, software; **Guobao Ma:** formal analysis, investigation; **Guobao Li:** data curation; **Zunce Wang:** writing-review and editing; **Yan Xu:** formal analysis, resources; **Yuejuan Yan:** data curation; **Jinglong Zhang:** preparation, visualisation.

References

Bai, W., Tijsseling, A. S., Wang, J., Duan, Q., & Zhang, Z. (2021). Large eddy simulation investigations of periodic cavitation shedding with special emphasis on three-dimensional asymmetry in a scaled-up nozzle orifice. *Journal of Fluids Engineering*, *143*(7). https://doi.org/10.1115/1.4050136

Bukharin, N., El Hassan, M., Omelyanyuk, M., & Nobes, D. (2020). Applications of cavitating jets to radioactive scale cleaning in pipes. *Energy Reports,6*, 1237-1243. https://doi.org/10.1016/j.egyr.2020.11.049

Cui, Y., Zhao, M., Ding, Q., & Cheng, B. (2024). Study on dynamic evolution and erosion characteristics of cavitation clouds in submerged cavitating water jets. *Journal of Marine Science and Engineering*, *12*(4), 641–641. https://doi.org/10.3390/jmse12040641

Dai, X., Wang, Z., Liu, F., Wang, C., Sun, Q., & Xu, C. (2019). Simulation of throttling effect on cavitation for nozzle internal flow. *Fuel, 243*, 277-287. https://doi.org/10.1016/j.fuel.2019.01.073

Dong, J., Li, S., Meng, R., Zhong, X., & Pan, X. (2022). Research on cavitation characteristics of two-throat nozzle submerged jet. *Applied Sciences, 12*(2), 536. https://doi.org/10.3390/app12020536

Fan, C. X., Li, D., Kang, Y., & Zhang, H. T. (2024). Effect of low-speed waterjet pressure on the rock-breaking performance of unsubmerged cavitating abrasive waterjet. *Petroleum Science*. https://doi.org/10.1016/j.petsci.2024.03.012

Han, C. Z., Xu, S., Cheng, H. Y., Ji, B., & Zhang, Z. Y. (2020). LES method of the tip clearance vortex cavitation in a propelling pump with special emphasis on the cavitation-vortex interaction.*Journal of Hydrodynamics, 32*(6), 1212-1216. https://doi.org/10.1007/s42241-020-0070-9

He, J., An, Q., Jin, J., Feng, S., & Zhang, K. (2023) Experimental study and simulation of cavitation shedding in diesel engine nozzle using proper orthogonal decomposition and large eddy simulation. *Journal of Thermal Science. 2023, 32*(4): 1487-1500. https://doi.org/10.1007/s11630-023-1817-8

Huang, G., Qiu, C., Song, M., Qu, W., Zhuang, Y., Chen, K., Huang, K., Gao, J., Hao, J., & Hao, H. (2024). Optimization of composite cavitation nozzle parameters based on the response surface methodology. *Water*, *16*(6), 850–850. https://doi.org/10.3390/w16060850

Li, L., Xu, Y., Ge, M., Wang, Z., Li, S., & Zhang, J. (2023). Numerical investigation of cavitating jet flow field with different turbulence models. *Mathematics,11*(18), 3977. https://doi.org/10.3390/math11183977

Liu, H., Xu, Y., Wang, Z., Zhang, J., & Wang, J. (2023). Experimental and numerical simulations to examine the mechanism of nozzle geometry affecting cavitation water jets. *Geoenergy Science*

and Engineering, *233*, 212511–212511. https://doi.org/10.1016/j.geoen.2023.212511

Liu, Y., Chen, X., Zhang, J., Feng, L., Liu, H., & Hao, C. (2024). Structural optimization design of ice abrasive water jet nozzle based on multi-objective algorithm. *Flow Measurement and Instrumentation*, *97*, 102586–102586. https://doi.org/10.1016/j.flowmeasinst.2024.102586

Peng, C., Tian, S., & Li, G. (2021). Determination of the shedding frequency of cavitation cloud in a submerged cavitation jet based on high-speed photography images. *Journal of Hydrodynamics*, *33*(1), 127–139. https://doi.org/10.1007/s42241-021-0016-x

Sekyi-Ansah, J., Wang, Y., Tan, Z., Zhu, J., & Li, F. (2020). The dynamic evolution of cavitation vacuolar cloud with high-speed camera. Arabian *Journal for Science and Engineering, 45*, 4907-4919. https://doi.org/10.1007/s13369-019-04329-0

Shan, M., Zha, Y., Yang, Y., Yang, C., Yin, C., & Han, Q. (2024). Morphological characteristics and cleaning effects of collapsing cavitation bubble in fractal cracks. *Physics of Fluids, 36*(6). https://doi.org/10.1063/5.0215048

Soyama, H. (2020). Cavitating jet: A review. *Applied Sciences,10*(20), 7280. https://doi.org/10.3390/app10207280

Świetlicki, A., Szala, M., & Walczak, M. (2022). Effects of shot peening and cavitation peening on properties of surface layer of metallic materials—a short review. *Materials, 15*(7), 2476. https://doi.org/10.3390/ma15072476

Trummler, T., Schmidt, S. J., & Adams, N. A. (2020). Investigation of condensation shocks and re-entrant jet dynamics in a cavitating nozzle flow by Large-Eddy Simulation. *International Journal of Multiphase Flow,125*, 103215. https://doi.org/10.1016/j.ijmultiphaseflow.2020.103215

Wang, J., Wang, Z., Cui, H., Liu, H., Yan, Y., Zhang, J., Li, S., & Xu, Y. (2025). Effects of jet impact angle on cavitation erosion intensity and cavitation cloud dynamics. *Ocean Engineering*, *315*, 119832. https://doi.org/10.1016/j.oceaneng.2024.119832

Wang, J., Wang, Z., Xu, Y., Liu, H., Yan, Y., Zhang, J., Li, S., & Ge, M. (2024). Analysis of the flow field characterization on the cavitation water jet applied to planar and curved surfaces. *Physics of Fluids, 36*(10). https://doi.org/10.1063/5.0233488

Xiang, L., Wei, X., & Chen, X. (2020) Experimental study on the frequency characteristics of self-excited pulsed cavitation jet. *European Journal of Mechanics - B/Fluids*, *83*. https://doi.org/10.1016/j.euromechflu.2020.04.006

Xu, Y., Liu, H., Wang, Z., Zhang, J., & Wang, J. (2024a). Analysis of the effects of nozzle geometry on the cavitation water jet flow field using orthogonal decomposition. *Iranian Journal of Science and Technology, Transactions of Mechanical Engineering, 48*(1), 119-132. https://doi.org/10.1007/s40997-023-00647-9

Xu, Y., Tian, J., Wang, Z., Zhang, J., Li, S., Yan, Y., & Ge, M. (2024b). A comprehensive study on the flow field of cylindrical cavitation nozzle jet under different turbulence models. *Ocean Engineering*, *315*, 119596–119596. https://doi.org/10.1016/j.oceaneng.2024.119596

Yang, Y., Li, W., Shi, W., Wang, C., & Zhang, W. (2020). Experimental study on submerged high-pressure jet and parameter optimization for cavitation peening. *Mechanika*, *26*(4), 346–353. https://doi.org/10.5755/j01.mech.26.4.27560

Yang, Y., Shi, W., Tan, L., Li, W., Chen, S., & Pan, B. (2021). Numerical Research of the Submerged High-Pressure Cavitation Water Jet Based on the RANS-LES Hybrid Model. *Shock and Vibration, 2021*(1), 6616718. https://doi.org/10.1155/2021/6616718

Yuan, X., Wang, N., Wang, W., Zhang, L., & Zhu, Y. (2022). Nozzle resonance mechanism and cooperative optimization of self-excited oscillating pulse cavitation jet. *Transactions of the Canadian Society for Mechanical Engineering,47*(1), 74-88. https://doi.org/10.1139/tcsme-2021-0092

Zhong, X., Dong, J., Liu, M., Meng, R., Li, S., & Pan, X. (2022). Experimental study on ship fouling cleaning by ultrasonic-enhanced submerged cavitation jet: A preliminary study. *Ocean Engineering, 258*, 111844. https://doi.org/10.1016/j.oceaneng.2022.111844